nature communications

Article

https://doi.org/10.1038/s41467-026-68411-6

In situ visualization of *Clostridioides difficile* phenotypic heterogeneity and single-cell morphology during gut infection

Received: 3 May 2025

Accepted: 2 January 2026

Published online: 14 January 2026

Check for updates

Nicholas V. DiBenedetto[1,2], M. Lauren Donnelly-Morell[1,2,3], Carol A. Kumamoto[1] & Aimee Shen[1]

Phenotypic heterogeneity refers to the ability of clonal populations of the same species to display distinct phenotypes despite experiencing the same environment. Bacteria exhibit phenotypic heterogeneity across diverse cellular processes, which can provide competitive fitness advantages both within the host and against surrounding microbiota. However, visualizing phenotypic heterogeneity at single-cell resolution within dense microbial communities is technically challenging. Here, we present a method for visualizing this heterogeneity by combining spectrally compatible reporters to track the spatial distribution of gene expression in individual bacterial cells in the mammalian gut. Using toxin gene expression in *Clostridioides difficile* as a model for visualizing phenotypic heterogeneity, we demonstrate that, while *C. difficile* primarily occupies the lumen, a subpopulation of *C. difficile* associates with the colonic epithelium independent of toxin production. We further show that heterogeneity in *C. difficile* toxin gene expression is independent of location in the gut and that a toxin gene overexpressing mutant unexpectedly forms filamentous cells during the acute phase of infection. Thus, our reporter system provides quantitative, single-cell resolution of bacterial behavior within the intact gut environment and establishes a broadly applicable platform for investigating phenotypic heterogeneity in dense microbial communities.

Localizing bacteria in their native context within a host has provided critical insights into host-microbe interactions and bacterial behavior in complex environments[1–5]. While methods such as fluorescence in situ hybridization (FISH) have visualized the spatial organization of bacterial species within tissues[6,7], these analyses do not provide information on the locations of phenotypically distinct subpopulations of a given species. Notably, fluorescent reporter strains have allowed phenotypic variation at the single-cell level in bacteria to be visualized in situ with minimal handling relative to techniques like RNA-FISH[8]. For example, *Vibrio cholerae* upregulates toxin genes during biofilm formation in the small intestine[9], *Yersinia pseudotuberculosis* spatially regulates virulence and detoxification gene expression in deep tissue sites[10,11], and *Mycobacterium tuberculosis* exhibits differential replication rates depending on its location within a caseous lesion[12,13]. While these analyses have revealed how specific bacterial sub-populations adapt to and interact with distinct microenvironments, the tissues infected by these bacteria have considerably lower microbial complexity than that found in the colon.

Historically, localizing bacteria in situ in the colon has been challenging due to the high density and dynamic nature of bacterial populations within this site[14,15]. While most FISH analyses have not localized specific bacterial species within the gut[7,16], fluorescent

[1]Department of Molecular Biology and Microbiology, Tufts University School of Medicine, Boston, MA, USA. [2]Program in Molecular Microbiology, Tufts University Graduate School of Biomedical Sciences, Boston, MA, USA. [3]Present address: Department of Pathology, Mass General Brigham, Harvard Medical School, Boston, MA, USA. e-mail: aimee.shen@tufts.edu

reporters have achieved visualization of individual *Bacteroides* spp. at the single-cell level in situ during colonization[17,18]. However, this work was done either in germ-free or weaning mice, which does not fully model the microbial complexity or immunocompetency of a conventional mouse model. Other studies have used fluorescent reporters to localize colonic pathogens like *Shigella sonnei* during infection, but these analyses have used non-natural infection routes and inocula[19] to facilitate the visualization of pathogens in situ.

Developing methods for visualizing phenotypic heterogeneity in situ in the colon would significantly advance our understanding of how specific bacterial species adapt to this densely populated and competitive environment[20]. Indeed, immense selective pressures promote the generation of phenotypically heterogeneous subpopulations[21]. For example, bacterial capsule genes in *Bacteroides*[22] and flagella and Type III secretion system genes in *Salmonella*[23,24] are heterogeneously expressed to promote colonization and virulence, respectively. Unfortunately, it has been technically challenging to reliably visualize phenotypic heterogeneity in situ in the colon, leaving questions about the frequency, spatial distribution, and selection of specific phenotypes during infection.

Visualizing phenotypic heterogeneity in the major nosocomial pathogen, *Clostridioides difficile*, is particularly relevant because numerous traits, such as flagellar motility, cell chaining, and sporulation, are heterogeneously expressed by this pathogen[21,25,26]. In addition, *C. difficile* expresses toxin genes in a bimodal manner in vitro[27], although the dynamics of toxin gene expression at the single-cell level during infection remain unclear. Understanding the location, frequency, and magnitude of toxin gene expression during infection is critical because toxin production is essential for disease[28], and the ability of toxins to bind their receptors on the colonic epithelium likely impacts disease severity[29]. In addition, toxin production is a critical factor for diagnosing *C. difficile* infection[30,31], but the location of its production could impact the progression of the disease.

To address these challenges, we developed fluorescent reporter strains for visualizing toxin gene expression at the single-cell level during the natural infection of conventional mice by *C. difficile*. We found that toxin gene expression is heterogeneously distributed in situ and that *C. difficile* is found in diverse anatomic regions in colonic sections, including in close association with the epithelial cell layer, a spatial localization that has not been previously described for *C. difficile* in conventional mice. Moreover, we discovered that (i) the relative localization of *C. difficile* within the colon does not strongly impact the frequency or magnitude of toxin gene expression and (ii) toxin production did not affect where *C. difficile* localizes in the colon. Remarkably, these imaging analyses revealed that a toxin gene overexpressing mutant forms filamentous cells during the acute phase of infection. Thus, our methodology provides a robust and streamlined workflow for visualizing phenotypic heterogeneity in *C. difficile*, which can likely be applied to other clostridial species. Our analyses further highlight how visualizing bacteria in situ can reveal previously unknown morphologies that are not captured in vitro, enhancing our understanding of microbial behavior and disease pathogenesis.

Results

Optimization of constitutive fluorescent reporters for visualizing *Clostridioides difficile*

To visualize the subset of *Clostridioides difficile* cells that express toxin genes during infection, we first developed spectrally compatible, constitutive fluorescent reporters that allow individual *C. difficile* cells to be visualized within a colonic section. Building upon chromosomally encoded constitutive *mNeonGreen* (*mNG*) reporters previously developed for *C. difficile*[32], we first sought to reduce the amount of mNG produced by the P_{slpA}*::LP-mNG* strain because its high-level mNG production caused toxicity at late stages of growth in vitro. To this end, we deleted the sequence encoding a leader peptide (*LP*) (Fig. 1a), which was previously shown to enhance the fluorescence of reporter constructs in *Bacteroides* spp[17]. Loss of the LP reduced P_{slpA}*::mNG* reporter fluorescence by 8-fold (Fig. 1b, c). We also tested a P_{gluD}*::mNG* reporter construct because RNA-Seq analyses indicated that this promoter is highly expressed during murine infection[33]. Indeed, *gluD* encodes a glutamine dehydrogenase that is used in diagnostic tests for detecting *C. difficile* infections[31]. The P_{gluD}*::mNG* reporter was 3-fold dimmer than the P_{slpA}*::mNG* reporter developed here, and it was also dimmer than the P_{cwp2}*::LP-mNG* reporter we previously developed[32] (Fig. 1b, c). Notably, aside from the P_{slpA}*::LP-mNG* strain, the *mNG* reporter strains exhibited uniform fluorescence and WT growth during broth culture (Fig. 1b–d).

In parallel, we optimized spectrally compatible *mScarlet*-based constitutive reporters. While we previously generated P_{cwp2}*::LP-mSc* and P_{slpA}*::LP-mSc* reporter strains[32], the recently developed mScarletI3 (mScI3) variant is ~3-fold brighter and matures more rapidly than mScarlet[34]. Notably, replacing the *mSc* reporter with the *mScI3* reporter increased fluorescence by 6-fold for the P_{cwp2} constructs (Fig. 2a–c). In the course of cloning the P_{cwp2}*::LP-mScI3* construct, we serendipitously determined that a G228R substitution enhanced the brightness of mScI3 in *C. difficile* by 2-fold (Fig. 2c). Expressing *mScI3* under the control of P_{slpA} without the leader peptide sequence increased the mean fluorescence by ~3-fold and led to more uniform fluorescence than the *mSc* reporters, likely because mScI3 matures faster than mSc[34]. Similar to our findings with the *mNG* reporter, the P_{gluD}*::mScI3* construct was the dimmest of the three promoter constructs tested (Fig. 2b, c). Importantly, high-level *mSc* or *mScI3* expression had minimal impact on bacterial growth even for the P_{slpA}-driven constructs (Fig. 2d).

Visualization of constitutive *C. difficile* fluorescent reporter strains in vivo

Having identified *mNG* and *mScI3* reporter constructs that allow for stable, robust fluorescence in vitro, we next tested whether the constitutive reporter strains could be visualized during murine infection. Eight-week-old antibiotic-treated, female C57BL/6 mice were orally gavaged with 1×10^6 *C. difficile* spores derived from reporter strains. Infected mice were sacrificed 48 h post-infection, when peak disease severity is typically observed[35]. Colonic tissues were harvested, embedded in OCT, and cryosectioned into 10 μm slices (Fig. 3a). Individual cells of the P_{gluD}*::mNG* and P_{slpA}*::mNG* reporter strains were readily seen (white arrows) in the colonic sections, with P_{slpA}*::mNG* being the brighter reporter (Fig. 3b), whereas the P_{cwp2}*::mNG* reporter strain was not reliably visualized (Supplementary Fig. 1). Individual cells of all three *mScI3* reporter strains were also readily detectable, with the *mScI3* reporters providing a better signal-to-noise ratio than the *mNG* reporters due to lower levels of autofluorescence from plant fiber in the red channel.

Similar to a prior report imaging *C. difficile* during murine infection using FISH[36], we found that most *C. difficile* cells were luminal, although cells in close association with the epithelium were readily detected, in contrast with this prior report[36]. *C. difficile* cells were also frequently found within a distinct border >50 μm above the epithelial layer (identified based on phalloidin staining); this localization was defined as mucosal (Fig. 3b). However, we were unable to directly visualize the mucus layer in these sections because preserving the mucus layer requires methacarn fixation, but this fixation method interferes with the fluorescence of the reporters[37,38]. Importantly, we observed these spatial distributions in multiple mice and multiple samples per mouse.

To ensure that the reporter strains were still capable of causing disease, we monitored the percent weight change of mice infected with *mNG* and *mSc(I3)* reporter strains relative to WT over the 48-h infection period, as well as their colonization levels in the cecum at the time of tissue harvest. Notably, the *mNG* strains caused similar levels of

https://doi.org/10.1038/s41467-026-68411-6

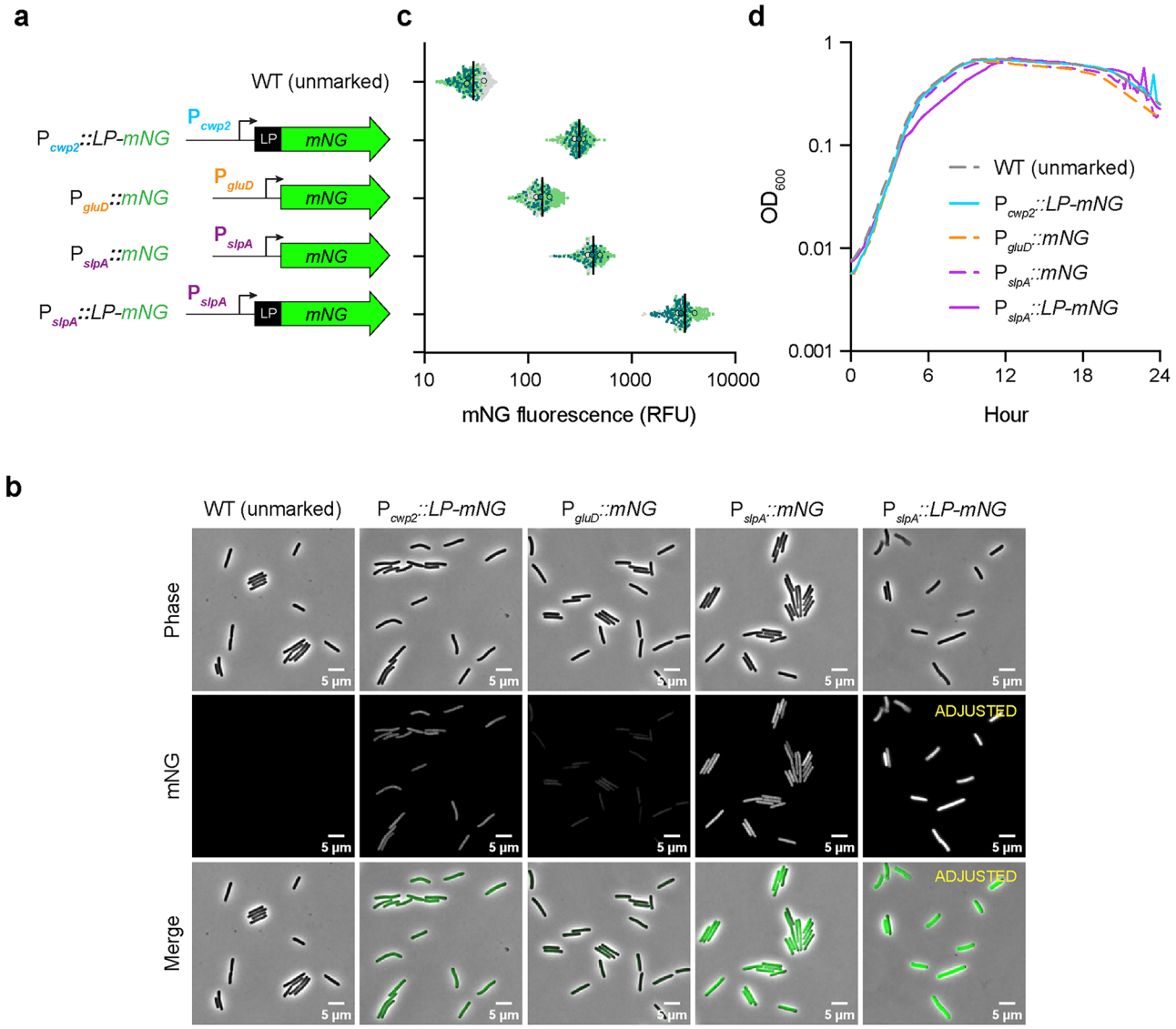

Fig. 1 | Optimization of constitutive *mNeonGreen* reporters. a Schematic of constitutive reporter constructs with the indicated promoters driving expression of *mNeonGreen* (*mNG*). LP encodes a leader peptide (*LP*) that functions to increase mNG levels. **b** Fluorescence microscopy of fixed cells expressing *mNG* grown to mid-log phase in BHIS broth culture. The mNeonGreen signal for P_{slpA}::*mNG* was reduced in images marked "ADJUSTED" because the reporter strain is 8–24-fold brighter than the other *mNG* reporter strains. Scale bar is 5 µm. Images are representative of three biological replicates. **c** Superplots of single-cell fluorescence intensity quantified using SuperSegger[64] for the strains shown in (**b**). The outlined colored dots represent the median fluorescence measured for a given biological replicate. The horizontal black line indicates the mean fluorescence value determined for three biological replicates (unmarked WT $n = 564$; P_{cwp2}::*LP-mNG* $n = 499$; P_{gluD}::*mNG* $n = 538$; P_{slpA}::*mNG* $n = 459$; P_{slpA}::*LP-mNG* $n = 327$). **d** Growth of the constitutive *mNG* reporter strains in BHIS broth based on optical density. A single biological replicate representative of three biological replicates is shown.

weight loss in mice (Fig. 3c) and colonized to similar levels as WT (Fig. 3d), indicating that the reporter constructs did not impair the infection process. Similar results were observed with *mSc*(*I3*) reporter strains, except that the P_{slpA}::*LP-mSc* reporter strain failed to cause disease (Fig. 3c) and P_{gluD}::*mScI3* and P_{slpA}::*LP-mSc(I3)* strains colonized at ~10-fold lower levels than WT (Fig. 3d).

Identification of *mNeonGreen* and *mScarletI3* reporter strains with WT fitness in vivo

We next measured the fitness of *mScI3* reporter strains capable of causing disease relative to WT by infecting mice with 50:50 mixes of WT and the P_{cwp2}::*LP-mScI3**, P_{gluD}::*mScI3*, or P_{slpA}::*mScI3* reporter strains. Competitive indices were determined based on the ratio of red fluorescent cecal CFUs to WT non-fluorescent cecal CFUs. The P_{cwp2}::*LP-mScI3** and P_{gluD}::*mScI3* strains exhibited equal fitness relative to WT, whereas the P_{slpA}::*mScI3* strain had a slight fitness defect (~3-fold, Fig. 4a). Similar levels of weight loss and colonization were observed for the competition infections as for the WT single-strain infection (Fig. 4b, c), except that the P_{gluD}::*mScI3* vs. WT and P_{slpA}::*mScI3* vs. WT competitions colonized to ~5–10-fold lower levels.

Since the auto-fluorescent nature of *C. difficile* in the green channel made it difficult to detect mNG-positive CFUs in a plate reader-based assay, we were unable to directly compare the fitness of *mNG* reporter strains to WT. Instead, we determined the relative fitness of P_{slpA}::*mNG* and P_{gluD}::*mNG* to P_{cwp2}::*LP-mScI3** and P_{gluD}::*mScI3* reporter strains, respectively (Fig. 4d). Similar levels of weight loss and colonization were observed for the competition infections as with the WT infections alone (Fig. 4e, f). Similar fitness levels were observed for P_{cwp2}::*LP-mScI3** and P_{slpA}::*mNG* strains, whereas the P_{gluD}::*mScI3* strain had a ~4-fold fitness advantage over P_{gluD}::*mNG* (Fig. 4d). While the P_{gluD}::*mScI3* and P_{gluD}::*mNG* reporter strains did not exhibit the highest fluorescence, we nevertheless determined their relative fitness in parallel with the

https://doi.org/10.1038/s41467-026-68411-6

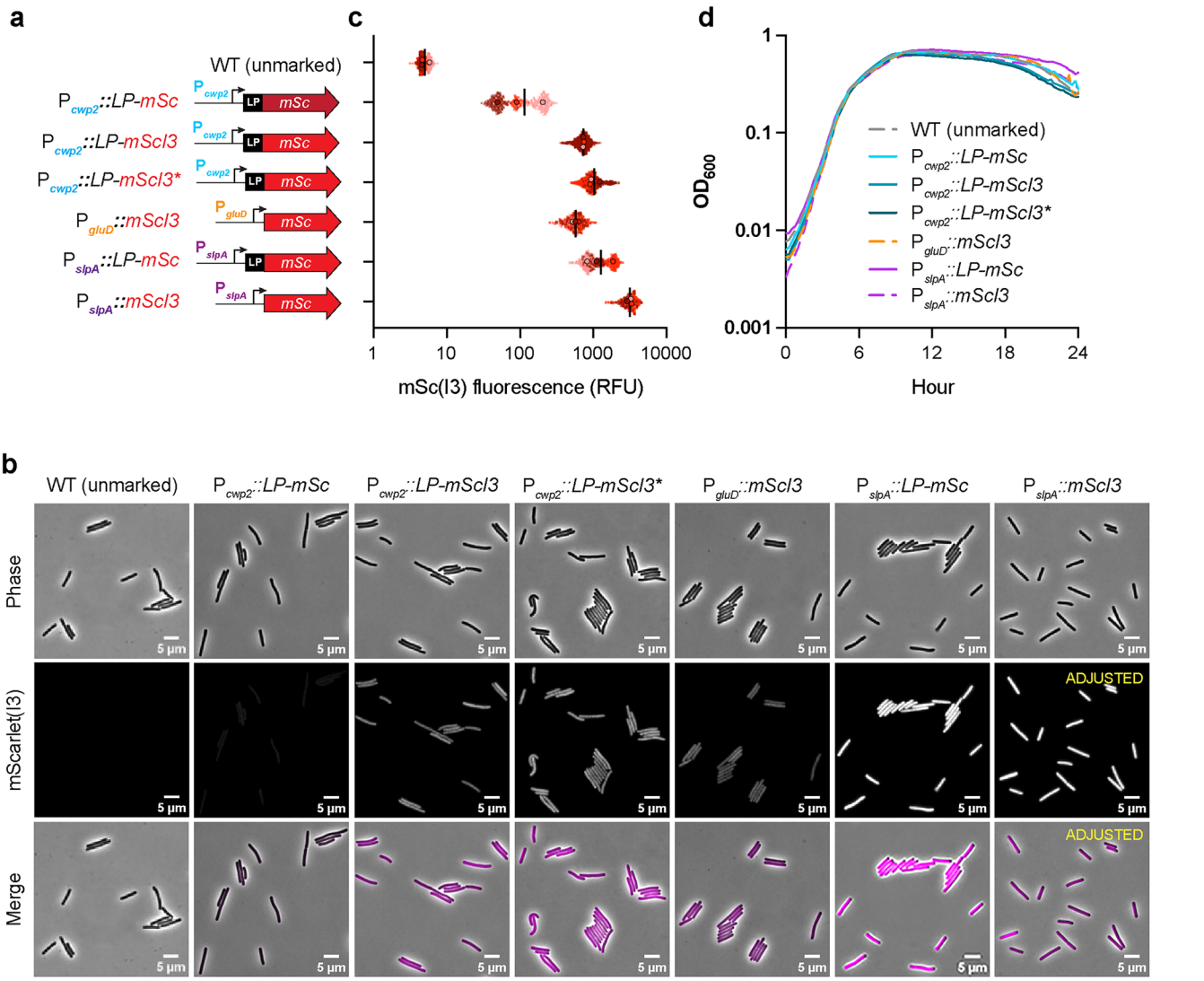

Fig. 2 | Optimization of constitutive *mScarlet(I3)* reporters. a Schematic of constitutive reporter constructs with the indicated promoters driving expression of *mScarlet* (*mSc*) or *mScarletI3* (*mScI3, * = mScI3 (G228R)*). *LP* encodes a leader peptide that functions to increase mSc(I3) levels. **b** Fluorescence microscopy of fixed cells expressing *mScarlet* or *mScarletI3*. The mScI3 signal was reduced in images marked with "ADJUSTED" because the P_{slpA}::*mScI3* reporter strain is 3–28-fold brighter than the other *mSc(I3)* reporter strains. Scale bar is 5 µm. Images are representative of three biological replicates. **c** Superplots of single-cell fluorescence intensity quantified using SuperSegger[64] for the strains shown in (**b**). The outlined colored dots represent the median fluorescence measured for a given biological replicate. The horizontal black line indicates the mean fluorescence value determined for three biological replicates (unmarked WT $n = 547$; P_{cwp2}::*LP-mSc* $n = 391$; P_{cwp2}::*LP-mScI3* n = 760; P_{cwp2}::*LP-mScI3** $n = 743$; P_{gluD}::*mScI3* $n = 443$; P_{slpA}::*LP-mSc* $n = 498$; P_{slpA}::*mScI3* $n = 376$). **d** Growth of the constitutive *mSc(I3)* reporter strains in BHIS broth based on optical density. A single biological replicate representative of three biological replicates is shown.

P_{cwp2}::*LP-mScI3** and P_{slpA}::*mNG* reporter pair to provide another potential option if the latter strain pair had a fitness defect.

Importantly, *mScI3* and *mNG* reporter cells were readily detected in colonic sections, and they exhibited equivalent spatial distributions in the lumen and close to the colonic epithelium, with green and magenta cells being similarly intermixed in these microenvironments (Fig. 4g). However, it was more challenging to detect the P_{gluD}::*mNG* strain because its signal is weaker relative to P_{slpA}::*mNG* (Fig. 4g). Taken together, these analyses identified P_{cwp2}::*LP-mScI3** and P_{slpA}::*mNG* reporters as the best red and green constitutive reporter strains to visualize during infection.

Development of dual reporter strains for visualizing phenotypic heterogeneity in toxin gene expression in situ during *C. difficile* infection

We next combined our optimized constitutive reporters with a toxin gene reporter to visualize the subset of cells expressing toxin genes in situ during infection. Specifically, we generated a dual reporter strain carrying the constitutive P_{cwp2}::*LP-mScI3* reporter with a toxin gene-specific *mNG* reporter that we previously constructed, P_{tcdA}::*mNG*[32]. The reporters were integrated into the chromosomes of WT, Δ*tcdR*, and Δ*rstA* strains at a neutral locus to assess the ability of the reporter system to read out toxin gene expression at the single-cell level. TcdR is the toxin gene-specific sigma factor that activates toxin gene expression, so toxin gene expression is essentially null in a Δ*tcdR* strain in vitro[32,39]. Conversely, RstA is a negative regulator of toxin gene expression, so a Δ*rstA* strain over-expresses toxin genes[40] and exhibits a higher frequency of toxin gene expression in vitro[32].

We first validated the bimodal nature of toxin gene expression in the dual reporter strains after overnight growth in TY broth (Fig. 5a; dual reporter strains are designated with an * from herein). While the constitutive *mScI3* reporter exhibited uniform fluorescence regardless of strain background (Fig. 5b), *tcdA* toxin gene expression was phenotypically heterogeneous, being observed in ~20% of cells in the WT*

https://doi.org/10.1038/s41467-026-68411-6

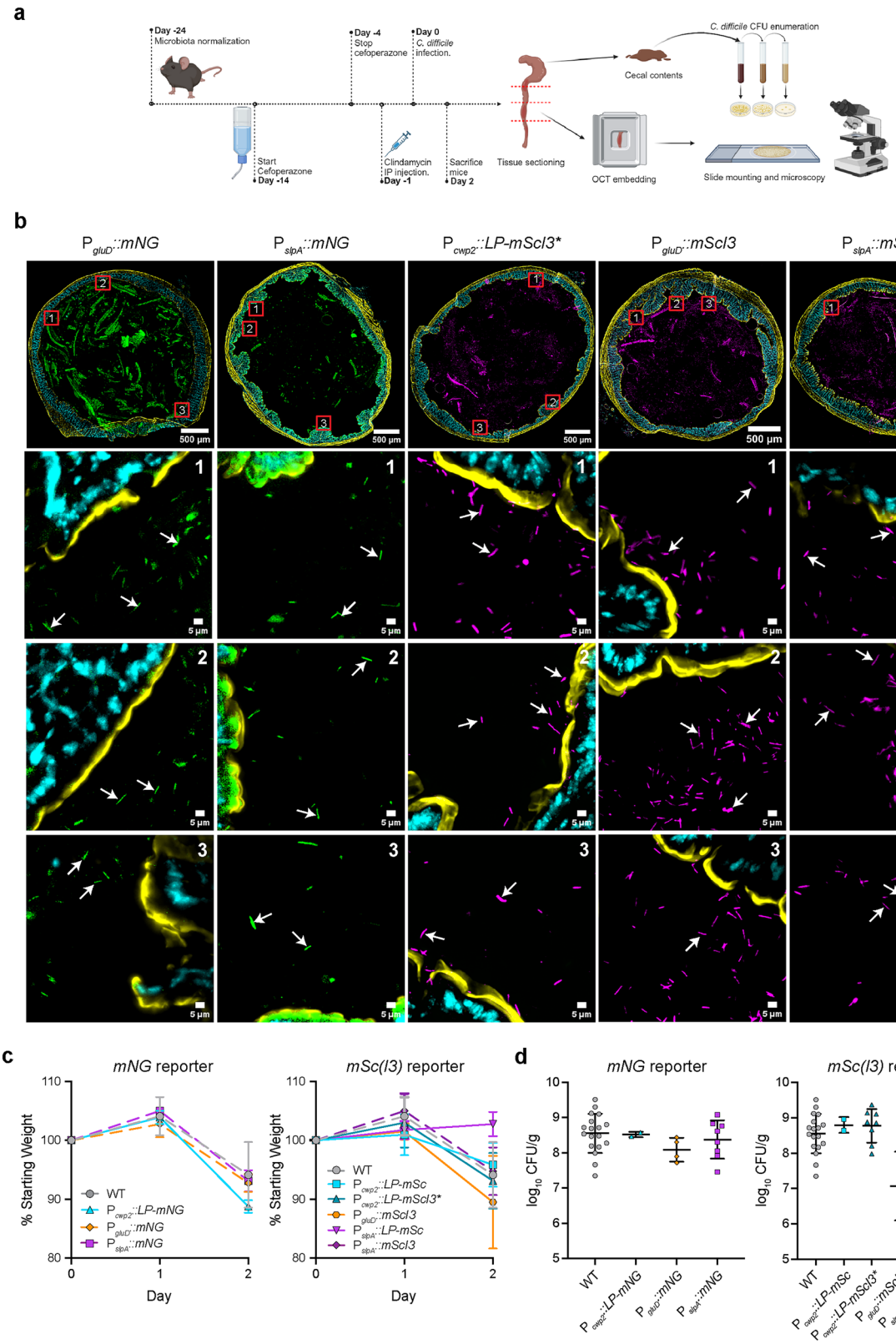

background (Fig. 5c, d). Toxin gene expression was ~2-fold higher (67%) and more frequent in the Δ*rstA** strain than in WT* (Fig. 5c, d), consistent with our prior analyses of toxin gene expression with single reporter strains[32]. To verify that the transcriptional reporters did not alter toxin production and that the toxin gene reporter fluorescence accurately reflects toxin production, western blot analyses were performed on cultures grown to the stationary phase in TY broth. These blots confirmed that the abundance of TcdA was unchanged in the reporter strains and that the fluorescent signal intensity correlated with protein concentration (Supplementary Fig. 2a, b).

When the dual reporter strains were used to infect mice, WT* and Δ*tcdR** colonized to similar levels, whereas Δ*rstA** colonized at ~4-fold lower levels than WT* on Day 2 post-infection (Fig. 6a). Despite this reduced colonization level on Day 2, the Δ*rstA** reporter strain

Fig. 3 | Validation of *mNeonGreen* and *mScarlet(I3)* reporters in vivo. **a** Schematic of mouse infection timeline and downstream analyses including *C. difficile* CFU enumeration, mouse colonic tissue preparation, sectioning, and slide mounting for microscopy. Created in BioRender. Kuhn, P. (2025) https://BioRender.com/hrn2umn. **b** Representative colonic section images of mice infected with constitutive reporter strains. Mice were infected with 1×10^6 spores and sacrificed on Day 2 (48 h) post-infection. Colon tissues were fixed in 4% PFA for 4 h prior to cross-sectioning and embedding in OCT blocks. 10 μm cryosections were taken and stained with Phalloidin (F-actin, yellow) and DAPI (nuclei, cyan). Numbers in the top right of each inset panel indicate the corresponding image on the tissue cross-section. White arrows highlight *C. difficile* cells expressing either *mNeonGreen* (*mNG*, green) or *mSarlet(I3)* (*mSc(I3)*, magenta, * = *mScI3 (G228R)*). The P_{slpA}::LP-*mSc* strain was not included in Fig. 3c because it failed to cause disease, and the P_{cwp2}::*mNG* strain was also excluded because its fluorescence was too low to be reliably detected. **c** Percent weight change of mice over the course of infection with the indicated *mNG* and *mSc(I3)* strains relative to the baseline weight measured at the time of infection (unmarked WT $n = 23$; P_{cwp2}::*LP-mNG* $n = 2$; P_{gluD}::*mNG* $n = 4$; P_{slpA}::*mNG* $n = 8$; P_{cwp2}::*LP-mSc* $n = 2$; P_{cwp2}::*LP-mScI3** $n = 8$; P_{gluD}::*mScI3* $n = 4$; P_{slpA}::*LP-mSc* $n = 4$; P_{slpA}::*mScI3* $n = 4$. Colored dots represent the mean, and error bars indicate standard deviation). **d** Cecal colony-forming units were measured on Day 2 (48 h) post-infection. Lines show the geometric mean and standard deviation. (unmarked WT $n = 18$; P_{cwp2}::*LP-mNG* $n = 2$; P_{gluD}::*mNG* n = 4; P_{slpA}::*mNG* $n = 8$; P_{cwp2}::*LP-mSc* $n = 2$; P_{cwp2}::*LP-mScI3** $n = 8$; P_{gluD}::*mScI3* $n = 4$; P_{slpA}::*LP-mSc* $n = 4$; P_{slpA}::*mScI3* $n = 4$).

nevertheless caused more weight loss in mice than the WT* reporter strain and unmarked WT strain (Fig. 6b). This virulence phenotype is consistent with prior work showing that an *rstA* mutant strain causes greater disease in hamsters, likely due to its higher toxin production, and colonizes to lower levels[41]. As expected, the Δ*tcdR* strain failed to cause weight loss (Fig. 6b).

To determine whether the reduced cecal CFU levels observed with the Δ*rstA** reporter strain were specific to acute infection or whether this strain exhibits colonization defects at later time points, we analyzed the infection dynamics of the dual reporter strains over the course of a 14-day infection. While the WT* and Δ*rstA** reporter strain and the unmarked WT strain caused similar levels of weight loss on Day 2, Δ*rstA** and the unmarked WT strains caused greater weight loss during peak disease severity between days 2 and 4 (10–20% of initial body weight) than the WT* reporter strain, which started to regain weight on Day 3 post-infection (Fig. 6b). Notably, by Day 14, the Δ*rstA** reporter strain achieved ~4-fold higher colonization levels than both WT strains tested ($p < 0.01$), despite colonizing at lower levels on Day 2 (Fig. 6a, $p < 0.01$).

Since the WT* reporter strain caused less weight loss than the unmarked WT strain on Days 3 and 4 post-infection, we sought to assess whether the Δ*rstA** reporter strain behaves differently from its unmarked parental Δ*rstA* strain by analyzing the weight loss of unmarked Δ*rstA* and an Δ*rstA*/*rstA* complementation strain. Importantly, the Δ*rstA* dual reporter strain caused similar levels of weight loss as the unmarked strains, indicating that the dual reporter does not affect the virulence of the Δ*rstA* strain. (Supplementary Fig. 3b).

To analyze toxin gene expression in the dual-reporter strains in colonic sections collected on Days 2 and 14 post-infection, we normalized the toxin gene expression fluorescence (P_{tcdA}::*mNG*) to the constitutive P_{cwp2}::*LP-mScI3** fluorescent signal observed within the same cell. This normalization provided a more uniform and accurate measure of fluorescence, correcting for variations caused by cells that were slightly out of focus within the image. When we compared the magnitude of toxin gene expression in the subset of cells identified as Toxin-ON, the Δ*rstA** reporter strain expressed toxin genes at ~1.6-fold higher levels on average than the WT* reporter strain on Day 2 (Fig. 6 d). Interestingly, the average magnitude of toxin gene expression for Toxin-ON cells was lower on Day 14 for the Δ*rstA** strain relative to Day 2. While Day 2 and Day 14 samples were harvested from different mice due to the endpoint nature of the assay, this trend was observed in two independent experimental infections (Fig. 6d). In contrast, there was little change in the magnitude of toxin gene expression for WT* cells between Day 2 and Day 14, although there was a slight decrease in the proportion of WT* cells expressing toxin genes on Day 14 (Fig. 6d, e). In both the WT* and Δ*rstA** strains, toxin gene expression was found to be heterogeneous during infection (Fig. 6c, d, e), with a higher proportion of Δ*rstA** reporter strain cells expressing toxin genes than WT* at Day 2 (57% vs. 20%, respectively, Fig. 6e), similar to our in vitro analyses (Fig. 5). As expected, the constitutive mScI3* reporter signal remained consistent across the dual reporter strains and between days 2 and 14 (Supplementary Fig. 4).

To address the possibility that *C. difficile* autofluoresces in the mNG or mScI3 channel or that autofluorescent debris in the gut might be mistaken for *C. difficile*, we infected mice with an unmarked WT strain. Tissues were harvested, processed, and imaged identically to infections with fluorescently tagged strains. Importantly, we did not observe autofluorescence of *C. difficile* in the mNG channel, suggesting that metabolites contributing to autofluorescence in *C. difficile* are not utilized during growth in the gut[42]. In addition, we only observed, on average, a few instances per section where fluorescence in the mScI3* channel could be mistaken for a *C. difficile* cell (Supplementary Fig. 5). Given that >1000 cells are readily visible in a given cross-section (using the constitutive P_{cwp2}::*mScI3** reporter construct), these rare "cells," which are <0.5% of the population analyzed, do not meaningfully affect the final data analysis. Nonetheless, it is critical to include an unmarked control to assess the degree to which non-specific debris might be mistaken for *C. difficile* cells during image analysis.

Relationship between toxin gene expression and spatial localization during infection

Since toxin production changes the metabolic environment surrounding *C. difficile* by liberating nutrients close to the epithelium[43], we asked whether toxin production impacts the localization of *C. difficile* within the colon. We found that the Δ*tcdR** strain exhibited similar spatial distributions in colonic sections relative to WT* and Δ*rstA** strains, with Δ*tcdR* being readily observed close to the epithelium (Fig. 6c, Supplementary Fig. 6). Thus, higher toxin gene expression does not appear to affect the proximity of *C. difficile* cells to the epithelium, at least under the conditions analyzed.

Since toxin gene expression is responsive to many environmental inputs[39], we assessed whether the magnitude and proportion of toxin gene-expressing cells are spatially or temporally regulated during infection. To this end, we grouped cells into three spatial categories, the lumen, mucosa, or epithelium, and measured the fluorescence of the P_{tcdA}::*mNG* reporter and quantified the magnitude and frequency of toxin gene expression (Fig. 7, Supplementary Fig. 7). These analyses revealed that neither the proportion of toxin gene-expressing cells nor the magnitude of their gene expression is affected by the proximity of *C. difficile* to the epithelium (Fig. 7, Supplementary Fig. 7).

Discovery of a filamentous cell morphology during acute infection by a mutant that over-expresses toxin genes

While no differences in the spatial distribution of *C. difficile* were observed between the WT*, Δ*tcdR**, and Δ*rstA** strains, we nevertheless discovered that the Δ*rstA* strain frequently forms curvy, filamentous cells on Day 2 (Fig. 6c, f, g Supplementary Fig. 6). Indeed, the Δ*rstA** reporter strain was ~1.5-fold longer on average than the WT* or Δ*tcdR** reporter strains, with some cells exceeding 50 μm. Notably, Δ*rstA** cells were more likely to be curved (19%) compared to WT* (3%) and Δ*tcdR** (7%) on Day 2, when peak weight loss is often observed (Fig. 6f, g). However, by Day 14, the percentage of curved Δ*rstA** cells decreased to 1.5%, which was similar to WT (Fig. 6g).

https://doi.org/10.1038/s41467-026-68411-6

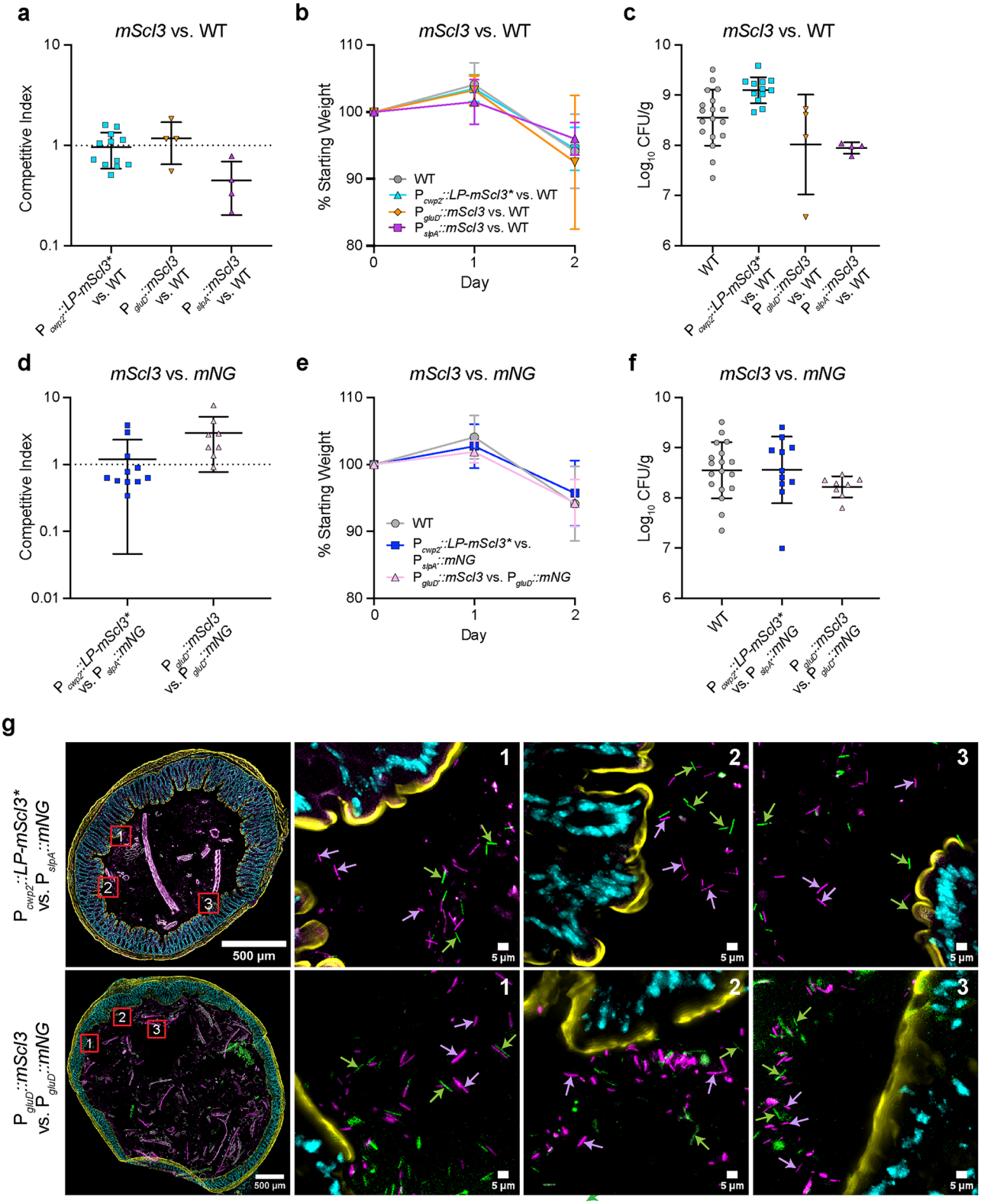

Since the abnormal cell morphologies observed for the Δ*rstA** reporter strains could be due to the over-expression of *mNG* in Δ*rstA** cells during peak infection, we analyzed the morphology of a Δ*rstA* strain expressing only the constitutive *mScl3* reporter (Supplementary Fig. 8). The Δ*rstA* single constitutive reporter strain was shorter than the Δ*rstA** dual reporter strain, but it was ~15% longer on average than the WT single reporter strain, although this difference was not statistically significant (Fig. 6f, Supplementary Fig. 8a, One-way ANOVA $F(5, 37) = 9.01$, $p < 0.0001$, $R^2 = 0.549$. Δ*rstA** vs Δ*rstA* single reporter (mean difference = 1.72, 95% CI [−0.79, 4.22], Tukey-adjusted $p = 0.329$). WT and Δ*rstA* single reporter (mean difference = −1.05, 95% CI [−3.99, 1.88], Tukey-adjusted $p = 0.887$)). Notably, the Δ*rstA* single reporter strain showed a trend toward forming more curved cells relative to the WT single reporter strain, similar to analyses of the Δ*rstA* dual reporter strain to WT and Δ*tcdR* dual reporter strains (Supplementary Fig. 8b).

Fig. 4 | Relative fitness of *mNeonGreen* and *mScarletI3* reporter strains in vivo. **a**, **d** Competitive indices of *mScI3*:WT or *mScI3*:*mNG* strains infections based on the red fluorescence of the resulting colonies. Lines show the geometric mean and standard deviation. (P_{cwp2}::*LP-mScI3** (* = G228R) $n = 12$; P_{gluD}::*mScI3* $n = 4$; P_{slpA}::*mScI3* $n = 4$; P_{cwp2}::*LP-mScI3** vs. P_{slpA}::*mNG* $n = 11$; P_{gluD}::*mScI3* vs. P_{gluD}::*mNG* $n = 8$; P_{cwp2}::*LP-mScI3** vs. P_{slpA}::*mNG* $n = 11$; P_{gluD}::*mScI3* vs. P_{gluD}::*mNG* $n = 8$). **b**, **e** Percent weight change of mice over the course of infection with the indicated competition infections and a WT control. Competition infections used 5×10^5 spores of each strain for a total infectious dose of 1×10^6 spores per mouse; 1×10^6 WT spores were used to infect mice as a control. Values are relative to the baseline weight measured at the time of infection (WT $n = 23$; P_{cwp2}::*LP-mScI3** vs. WT $n = 12$; P_{gluD}::*mScI3* vs. WT $n = 4$; P_{slpA}::*mScI3* vs. WT $n = 4$). **c**, **f** Cecal colony-forming units measured Day 2 (48 h) post-infection from the infections shown in (**b**, **e**). Lines show the geometric mean and standard deviation. **g** Representative images of mice co-infected with either P_{cwp2}::*LP-mScI3** and P_{slpA}::*mNG* (top) or P_{gluD}::*mScI3* and P_{gluD}::*mNG* (bottom) from samples harvested Day 2 post-infection. 10 μm cryosections were stained with Phalloidin (F-actin, yellow) and DAPI (nuclei, cyan). Numbers in the top right of each inset panel indicate the corresponding image on the tissue cross-section. Green and mauve arrows indicate *C. difficile* cells expressing either *mNeonGreen* (*mNG*, green) or *mScarletI3* (*mScI3*, magenta), respectively.

To assess if over-expression of the toxin genes alone, irrespective of the toxin gene reporter, contributes to the increase in elongated and/or curved cells, we compared the cell morphologies of a Δ*rstA*Δ*tcdR** dual reporter strain to the Δ*rstA* single constitutive gene reporter and Δ*rstA** dual reporter strains. While the Δ*rstA*Δ*tcdR** dual reporter strain colonized to similar levels as the unmarked WT strain and did not induce weight loss in mice (Supplementary Fig. 3a, b), the double mutant strain produced cells that were slightly shorter and less curved than the Δ*rstA* single reporter strain and significantly shorter than the Δ*rstA** dual reporter cells (-1.3-fold, Δ*rstA** vs Δ*rstA*Δ*tcdR**: mean difference = 2.16, 95% CI [0.37, 3.95], $p = 0.010$) on average (Supplementary Fig. 8a). While this altered morphology appears to be linked to high-level toxin gene expression, it does not appear to be the sole driver of this phenotype because cells expressing P_{tcdA}::*mNG* to high levels were more likely to be elongated in the *ΔrstA* strain background, whereas in the WT background, these cells were more likely to be shorter in the WT strain (Supplementary Fig. 9). Thus, while high-level mNG production exacerbates the morphological changes in the Δ*rstA* reporter strain, it is not solely responsible for the morphological abnormalities observed with the Δ*rstA* mutant on Day 2 of infection. These data imply that loss of RstA, irrespective of toxin gene expression, contributes to the curvy, elongated cell morphology observed in the Δ*rstA* strain backgrounds during the acute stages of infection.

Since the elongated morphology of the Δ*rstA** strain was only observed during the acute stage of infection, we sought to determine whether different phases of growth in vitro or minimal media conditions could also induce this phenotype. To this end, we grew WT, Δ*tcdR*, and Δ*rstA* dual reporter strains in nutrient-rich TY or minimal CDDM media and imaged cells at mid-log or stationary phase. No morphological differences across strains or conditions were detected (Supplementary Fig. 10a, b), and the magnitude and frequency of toxin gene expression in each strain were similar within growth phases across different media conditions (Supplementary Fig. 10c). Thus, the abnormal morphology of the Δ*rstA** strain appears to be specific to the acute phase of murine infection.

Discussion

Phenotypic heterogeneity allows bacteria to maximize their fitness in dynamic environments[44] such as those found in the gut[15,45], but it has been challenging to image this heterogeneity at the single-cell level in the dense colonic environment in situ. Here, we developed chromosomally encoded, spectrally compatible fluorescent reporters that allow us to visualize the subset of *C. difficile* cells expressing toxin genes in situ during murine infection. Moreover, our approach could be applied to study heterogeneity in gene expression in situ for the many colonization and virulence factors that *C. difficile* expresses in a bimodal manner[25,32,33,46].

Our analyses also advance our understanding of the spatial and temporal dynamics of toxin gene expression during *C. difficile* infection. First, they revealed that, while *C. difficile* is primarily a luminal pathogen, a sub-population is proximal to the epithelial layer, and a minority of this sub-population directly interacts with the epithelium (Figs. 3–7). Second, they demonstrated that a cell's location relative to the colonic epithelium does not affect the magnitude or frequency of toxin gene expression, and toxin gene expression does not grossly affect where *C. difficile* is localized within the colon (Fig. 7, Supplementary Fig. 7). Third, they showed that the frequency and magnitude of toxin gene expression does not change over time, except in the Δ*rstA* strain, where toxin genes were expressed at lower levels and less frequently 14 days post-infection compared to 2 days post-infection within this strain background (Fig. 6d, e). This could represent an adaptation by the Δ*rstA* strain or a selection for cells expressing toxin genes at lower levels.

Based on these observations, *C. difficile* likely uses heterogeneity in toxin gene expression as a bet-hedging strategy to partition the metabolically intensive task of toxin production so that non-toxin-producing cells, and ultimately the entire population, can benefit[25,45,47]. Specifically, the ability of toxin-producing cells to damage the host epithelium and release nutrients likely benefits non-toxin-producing cells by freeing this sub-population from the metabolic costs of toxin synthesis. Non-toxin-producing cells may then allocate resources toward processes such as specific metabolic programs or sporulation, a critical step in disease dissemination. Indeed, we previously reported a division of labor between toxin production and sporulation during the growth of *C. difficile* under certain conditions in vitro[32]. Consistent with this hypothesis, the Δ*rstA* mutant's reduced colonization levels (Fig. 6a) could suggest that overproducing toxin decreases *C. difficile*'s ability to expand in the gut during the acute phase. Alternatively, it may also reflect filamentous cells producing fewer colonies on a plate. Regardless, given RstA's multiple roles in regulating sporulation, toxin production, and motility[40,41], testing our hypothesis would require mutants that independently overexpress toxin genes.

Our analyses also highlight a key benefit of localizing bacteria at the single-cell level in situ because we serendipitously discovered that the Δ*rstA* strain adopts a filamentous, curved morphology specifically during the acute phase of infection. This abnormal morphology may be due to stressful conditions encountered during this infection phase because Δ*rstA* cells grown in TY or minimal media broth exhibit WT cell morphology despite expressing toxin genes (and the *mNG* reporter gene) to high levels (Supplementary Fig. 10). The specific conditions responsible for this phenotype remain unclear, but stressors that are present during infection, such as oxidative stress, induce DNA replication arrest through *C. difficile's* SOS response, which can cause cell filamentation[48].

Notably, our identification of spectrally compatible constitutive reporter strains with equivalent fitness (P_{cwp2}::*LP-mScI3** and P_{slpA}::*mNG*) will enable future studies focused on identifying genes that impact the relative spatial distribution of *C. difficile* cells in the colonic epithelium. Indeed, our analyses are the first to show that a subpopulation of *C. difficile* is found in close proximity to the epithelium (Figs. 3–7). This previously unappreciated subpopulation may be important for delivering *C. difficile*'s toxins more efficiently to their receptors or for establishing biofilms that promote recurrent infections. In addition, the epithelium-associated subpopulation could be responsible for generating spores that are more readily taken up by epithelial cells, which can serve as a reservoir for seeding recurrent infections[49]. Moreover, since genes important for this localization to the epithelium remain unknown, our reporter system should facilitate the identification of these genes by

https://doi.org/10.1038/s41467-026-68411-6

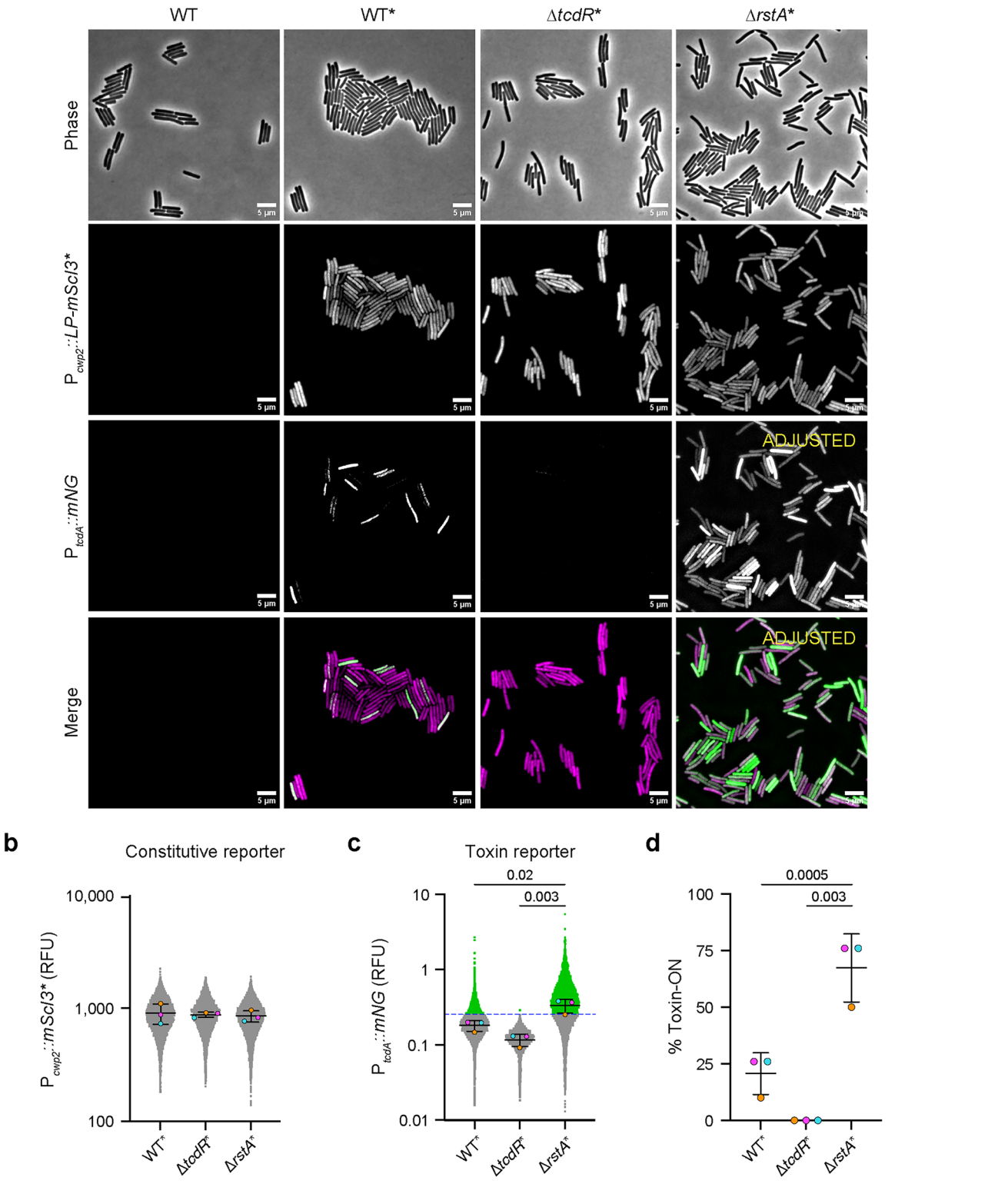

analyzing the relative distribution of *mScI3* and *mNG* reporter strains in different mutant backgrounds during single or competitive infections. The constitutive reporter pairs can also be used to analyze founder effects[17,50], such as whether avirulent strains can outcompete virulent strains by inhabiting different spatial niches at early stages of infection[51] or whether two strains exhibit different distributions during long-term colonization or recurrent infections.

The spectrally compatible reporters that we have optimized for use in *C. difficile* may also enable analyses of the division of labor between phenotypically heterogeneous traits, such as the overlap between toxin gene-expressing and sporulation-inducing cells, which we previously showed can occur under certain growth conditions in the lab[32]. However, addressing this particular possibility will require the development of alternative methods for visualizing all *C. difficile*

Fig. 5 | Toxin gene expression in dual reporter strains during growth in broth culture. a Representative fluorescence microscopy of unmarked WT or dual reporter strain cells (*mScI3* = *mScarletI3*; *mNG* = *mNeonGreen*; * = P_{cwp2}::*LP-mScI3*-G228R /P_{tcdA}::*mNG* dual reporters) grown to the stationary phase in TY broth. The mNeonGreen signal for the P_{tcdA}::*mNG* reporter in Δ*rstA** was decreased (marked as ADJUSTED) so that differences in P_{tcdA}::*mNG* reporter expression between WT* and Δ*rstA** could be visualized. Scale bar = 5 μm. Magenta = P_{cwp2}::*LP-mScI3**, Green = P_{tcdA}::*mNG*. **b**, **c** Superplots of single-cell mean fluorescence intensity for P_{cwp2}::*LP-mScI3** (**b**) and P_{tcdA}::*mNG*/P_{cwp2}::*LP-mScI3*-G228R (**c**) quantified using SuperSegger[64] from the strains shown in (**a**). The outlined colored dot represents the median fluorescence measured for a given biological replicate. The horizontal black line indicates the mean fluorescence determined for three biological replicates. The dotted blue line in **c** is used to define Toxin-ON in (**d**). The % Toxin-ON (green dots) was determined by the proportion of cells with mNeonGreen signal greater than the highest P_{tcdA}::*mNG* signal in the Δ*tcdR** dual reporter strain. Values that are separated above the clustering of points within the Δ*tcdR** datasets are considered toxin-ON. (for **b**, **c** WT* $n = 6244$; Δ*tcdR** $n = 4358$; Δ*rstA** $n = 7346$). **d** Percentage of cells expressing the toxin-specific P_{tcdA}::*mNG* reporter in the indicated dual reporter strains. Mean and standard deviation are shown for three biological replicates. Statistical significance was determined using a one-way ANOVA and Tukey's test. For superplots, statistical analyses were done on median values. Only statistically significant comparisons are shown.

cells, such as a constitutive reporter that fluoresces in the blue channel or an antibody that exclusively recognizes *C. difficile* in the gut environment. Unfortunately, FISH approaches are unlikely to be compatible with the fluorescent proteins optimized here due to the permeabilization and denaturing steps often needed to allow DNA probe access[52]. We attempted to use genetically encoded fluorescent proteins with greater stability, like StayGold[53], hfYFP[54], and GreenLantern[55], in *C. difficile*, but they did not exhibit sufficient fluorescence in *C. difficile* to proceed to animal studies. A similar limitation of our fluorescent reporter system is its incompatibility with standard methods for visualizing mucins, which require methacern fixation[38]. Additionally, there are challenges in visualizing a non-adherent bacterium like *C. difficile* within colonic sections; for example, *C. difficile* is more reliably visualized in tissue sections with a fecal pellet. Another potential limitation is the use of weight loss as a relatively indirect indicator of infection, as it can be influenced by multiple factors beyond toxin abundance. Including additional measures of pathogenicity could provide greater insight into factors affecting disease progression.

Regardless, since promoters in other clostridia are efficiently used in *C. difficile* and vice versa[56–60], our approach opens the door for investigating not only the spatial and temporal regulation of gene expression during infection by *C. difficile* but also other clostridial organisms that modulate gut health or disease. Given the critical role of clostridial organisms in maintaining gut health[61], the ability to analyze the spatial and temporal dynamics of their colonization and gene expression will enable mechanistic insights into their impacts on the gut microbiome and human health.

Methods

All animal studies were done with prior approval from the Tufts Institutional Animal Care and Use Committee (IACUC protocol #B2024-30).

Bacterial strains and growth conditions

All *C. difficile* strains used for this study are listed in Supplementary Table 1. All constructed strains derive from the sequenced clinical isolate 630, with the erythromycin-sensitive 630Δ*erm*Δ*pyrE* serving as the parental strain for all strain constructions using *pyrE*-based allele-coupled exchange (ACE)[62]. Strains were grown on brain heart infusion supplemented with yeast extract and cysteine (BHIS); taurocholate (TA; 0.1% [wt/vol]; 1.9 mM), cefoxitin (8 mg/mL), thiamphenicol (10 to 15 mg/mL), and kanamycin (50 mg/mL) were added as needed. For ACE, the *C. difficile* defined medium (CDDM)[63] was supplemented with 5-fluoroorotic acid (5-FOA; 2 mg/mL) and uracil (5 mg/mL). All *C. difficile* strains were first grown overnight from glycerol stocks on BHIS plates supplemented with TA (0.1% [wt/vol]).

Escherichia coli strains used for HB101/pRK24-based conjugations are listed in Supplementary Table 1. *E. coli* strains were grown at 37 °C with shaking at 225 rpm in Luria-Bertani (LB) broth. The medium was supplemented with ampicillin (50 mg/mL) and chloramphenicol (20 mg/mL) as needed.

C. difficile strain construction

Single-reporter strains were generated by conjugating HB101 carrying pMTL-YN1C plasmids into Δ*pyrE*-based strains using ACE. To generate dual-reporter strains, constitutive reporters were introduced downstream of the *sipL* locus of 630Δ*erm*Δ*pyrE*, 630Δ*erm*Δ*tcdR*Δ*pyrE*, or 630Δ*erm*Δ*rstA*Δ*pyrE* using ACE and pMTL-YN3-P_{cwp2}::*LP-mScarlet(I3)*. The second reporter, P_{tcdA}::*mNeonGreen*, was then introduced into the *pyrE* locus of the resulting strains using pMTL-YN1C-P_{tcdA}::*mNeonGreen*. At least two clones of each strain generated by allelic exchange were phenotypically characterized prior to restoration of the *pyrE* locus using pMTL-YN1C. All primer sequences can be found in Supplementary Table 2.

Growth curves

C. difficile cultures were grown in 2 mL BHIS medium to the stationary phase and then were back-diluted 1:50 in 2 mL BHIS and grown until an OD_{600} of 0.5 was reached. All strains were normalized to an OD_{600} of 0.5 if growth rates varied. Next, strains were diluted into 200 μL of BHIS broth in a 96-well plate to a starting OD_{600} of 0.05. Each strain was grown in technical triplicate alongside BHIS blanks. Plates were read in an Epoch plate reader (BioTek) in the anaerobic chamber with OD_{600} readings performed every 15 min after a 2-min linear shake. For in vitro toxin visualization, *C. difficile* cultures were grown in 2 mL TY broth to mid-log phase, then back-diluted 1:50 in 2 mL TY and grown overnight, followed by fixation and microscopy.

Cell fixation of broth-grown cultures

Cells were grown to mid-log phase in BHIS broth or to stationary phase in TY broth overnight. Next, 500 μL of culture was added directly to a tube containing 120 μL of a 5× fixation cocktail (100 μL of 16% [wt/vol] paraformaldehyde aqueous solution [methanol-free]) and 20 μL of 1 M $NaPO_4$ buffer (pH 7.4). The samples were mixed and incubated aerobically for 30 min at room temperature in the dark, followed by 30 min on ice in the dark. The fixed cells were washed 3 times in phosphate-buffered saline (PBS) and resuspended in 500 μL (depending on the density of the culture). Two μL of fixed cells were spotted onto a 1.5% agarose pad. Once the spot of cells was dry, a coverslip was added to seal the slide, and the slide was incubated at 37 °C for 2 h to allow for fluorophore maturation before imaging.

Western blots

Cells were grown to the stationary phase, and 3 mL of culture was then lysed by freeze-thawing. 20 μL of lysate was then loaded onto a 7.5% SDS-PAGE gel. Proteins were transferred to polyvinylidene difluoride membranes, which were subsequently probed with mouse (anti-TcdA, 1 mg/mL, 1:5000 dilution, Novus Biologicals) and chicken (anti-glutamate dehydrogenase, 2 mg/mL (1:10,000 dilution, Thermo Scientific) primary antibodies, followed by goat anti-mouse IR680 and donkey anti-chicken IR800 (LI-COR Biosciences, 0.5 mg/mL 1:30,000 dilution) secondary antibodies, respectively. Blots were imaged using a LiCor Odyssey CLx imaging system. The results shown are representative of multiple experiments.

https://doi.org/10.1038/s41467-026-68411-6

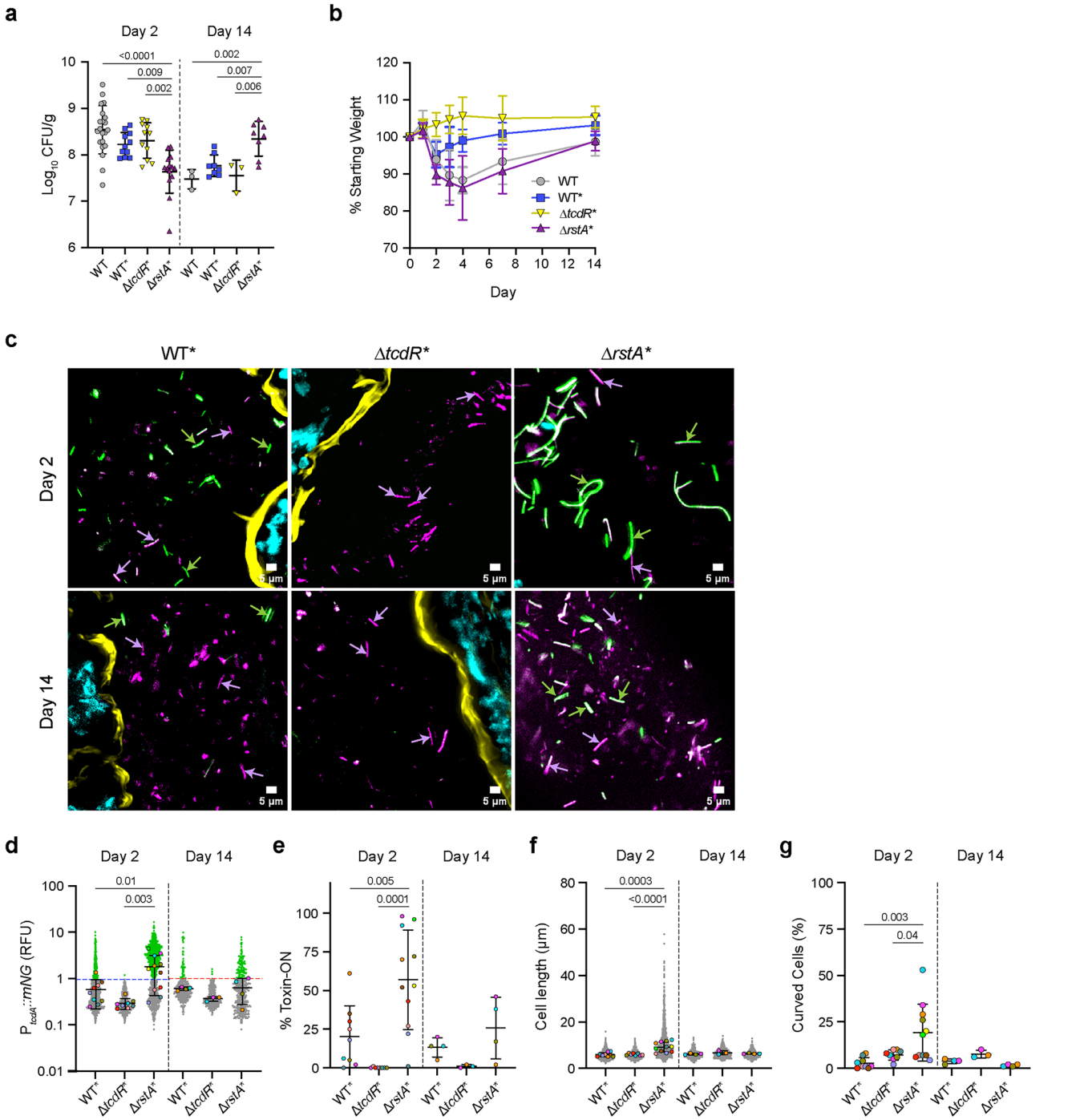

Fig. 6 | In situ analyses of phenotypic heterogeneity in toxin gene expression during murine infection reveal that a toxin gene-overexpressing mutant forms filaments during the acute phase of infection. a Cecal colony-forming units measured at Day 2 or Day 14 post-infection for WT, WT*, Δ*tcdR**, and Δ*rstA** strains (*mScI3* = *mScarletI3*-G228R; *mNG* = *mNeonGreen*; * denotes dual reporter strains carrying P_{cwp2}::*LP-mScI3*-G228R and P_{tcdA}::*mNG*). Lines indicate mean ± s.d. Day 2: Tukey's test; WT vs Δ*rstA**: mean difference = 0.90, 95% CI [0.50, 1.30], adjusted $p < 0.0001$; WT* vs Δ*rstA**: 0.58 [0.11, 1.06], $p = 0.0093$; Δ*tcdR** vs Δ*rstA**: 0.67 [0.20, 1.14], $p = 0.0022$. At Day 14: WT vs Δ*rstA**: −0.87 [−1.45, −0.29], $p = 0.0026$; WT* vs Δ*rstA**: −0.58 [−1.01, −0.15], $p = 0.0065$; Δ*tcdR** vs Δ*rstA**: 0.79 [0.21, 1.37], $p = 0.0058$. b. Percent weight change over the course of infection following inoculation with 1×10^6 spores of the indicated strains, normalized to baseline weight. **c** Representative colonic cross-sections from mice infected with WT*, Δ*tcdR**, or Δ*rstA** strains at the indicated time points. Tissues were fixed in 4% PFA, embedded in OCT, sectioned (10 μm), and stained with phalloidin (F-actin, yellow) and DAPI (nuclei, cyan). Green arrows indicate Toxin-ON cells; mauve arrows indicate Toxin-OFF cells expressing only the constitutive reporter. d. Superplots of normalized toxin reporter fluorescence (P_{tcdA}::*mNG*/P_{cwp2}::*LP-mScI3*-G228R) at the single-cell level in colonic sections at Day 2 or Day 14 post-infection. The Toxin-ON threshold was defined as values exceeding the highest normalized signal observed in Δ*tcdR** cells (dashed blue line, Day 2; dashed red line, Day 14). **e** Percentage of Toxin-ON cells per strain; mean ± s.d. is shown (≥100 cells quantified per mouse). **f** Superplots of single-cell lengths measured in colonic sections. Median values from 100 cells per mouse are shown (outlined points), with the mean of medians indicated (horizontal line). Δ*rstA** cells were significantly longer than WT* and Δ*tcdR** cells (WT* vs Δ*rstA**: −3.30 [−4.96, −1.64], adjusted $p = 0.0001$; Δ*tcdR** vs Δ*rstA**: −3.21 [−4.93, −1.50], $p = 0.0003$). **g** Percentage of curved cells per strain (mean ± s.d.). Statistical significance was determined by one-way ANOVA with Tukey's multiple-comparisons test; only significant comparisons are shown.

https://doi.org/10.1038/s41467-026-68411-6

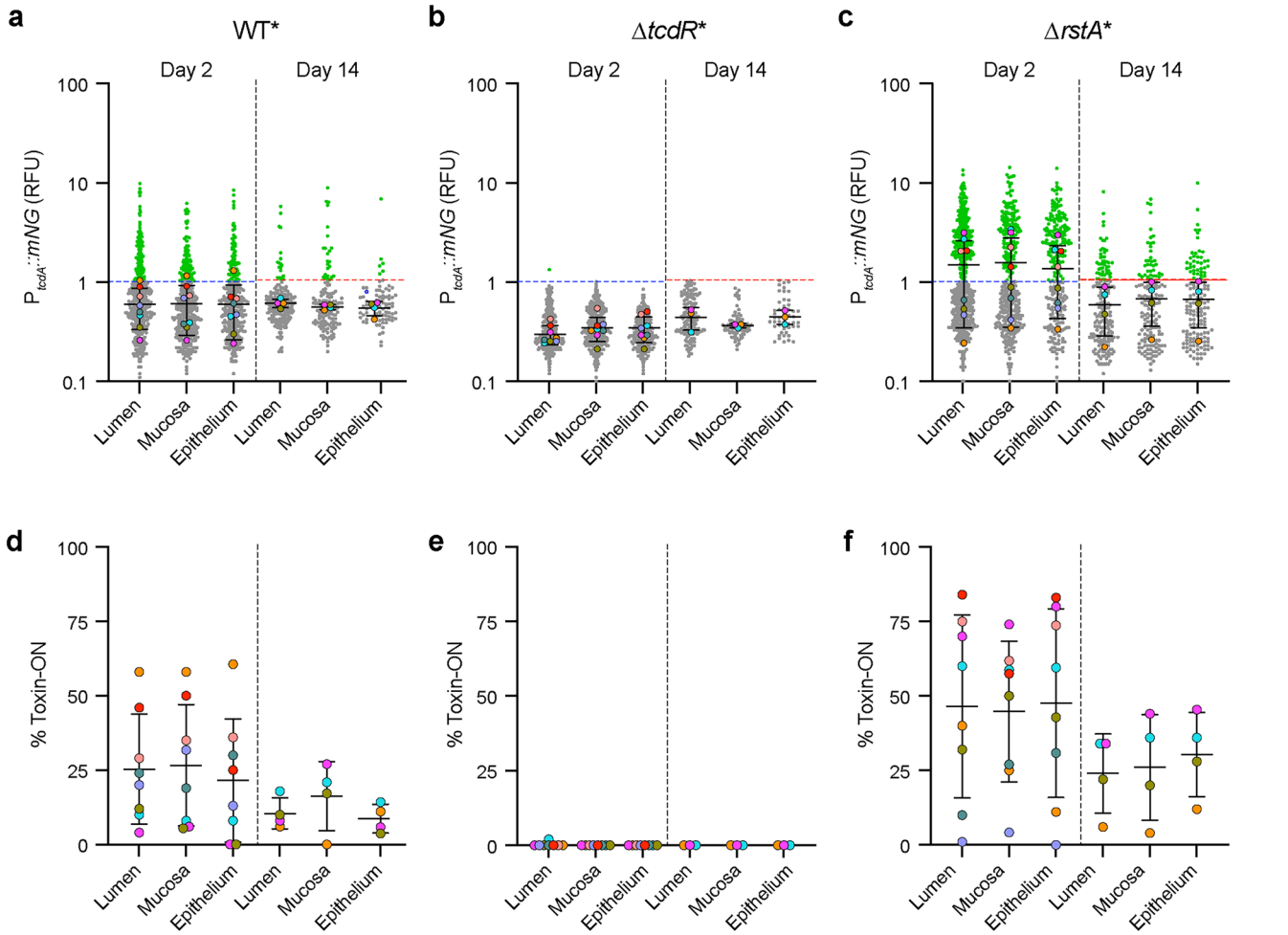

Fig. 7 | Spatial distribution of toxin gene expression during murine infection. **a**–**c** Single-cell quantification of toxin gene-specific fluorescence (P_{tcdA}::*mNG*) normalized to the constitutive P_{cwp2}::*LP-mScI3*-G228R signal was performed across *C. difficile* cells localized to the lumen, mucosa, and epithelium of infected mice (* denotes dual reporter strains carrying P_{cwp2}::*LP-mScI3*-G228R and P_{tcdA}::*mNG*). Each gray point represents an individual bacterium. Superplots with colored points denote the median fluorescence value per mouse. Horizontal black lines indicate the mean and standard deviation of medians. Dashed lines mark the negative-control threshold used to define toxin-ON cells on day 2 (blue) and day 14 (red). **d**–**f** The % Toxin-ON (green dots in **a**–**c**) was determined by the proportion of cells with mNeonGreen signal greater than the highest P_{tcdA}::*mNG* signal in the Δ*tcdR** dual reporter strain. Values that are separated above the clustering of points within the Δ*tcdR** datasets are considered toxin-ON. For Day 2 infections, $n = 8$ mice per strain were analyzed. For mice infected with the WT dual reporter strain, a total of 1219 cells were counted, including 500 luminal, 373 mucosal, and 346 epithelial bacteria. For mice infected with the Δ*tcdR* dual reporter strain, a total of 831 cells were counted, comprising 325 luminal, 282 mucosal, and 224 epithelial bacteria. For mice infected with the Δ*rstA* dual reporter strain, a total of 1162 cells were counted, including 555 luminal, 344 mucosal, and 263 epithelial bacteria. For Day 14 infections, $n = 4$ mice for WT and Δ*rstA* and $n = 3$ mice for Δ*tcdR* were analyzed. For mice infected with the WT dual reporter strain, a total of 409 cells were counted, comprising 189 luminal, 139 mucosal, and 81 epithelial bacteria. For mice infected with the Δ*tcdR* dual reporter strain, a total of 275 cells were counted, including 150 luminal, 75 mucosal, and 50 epithelial bacteria. For mice infected with the Δ*rstA* dual reporter strain, a total of 497 cells were counted, comprising 200 luminal, 150 mucosal, and 147 epithelial bacteria. Statistical significance was determined using a one-way ANOVA and Tukey's test on median values. Only statistically significant comparisons are shown. To see per mouse counts at each location, see Supplementary Fig. 6.

Murine infections

All mouse experiments were performed under the guidance of veterinary staff within the Tufts Comparative Medicine Services (TCMS) core. Seven-week-old female C57BL/6 cage-mate mice (Jackson Laboratory) were housed together in a large sterile rat cage to allow microbiota normalization over a 10-day period. Mice were fed irradiated Lab Diet 2918 throughout. After 10 days, cefoperazone (0.5 mg/mL) was added to the drinking water, which was provided ad libitum for another 10 days. Mice were then returned to sterile drinking water for 2 days before receiving a single intraperitoneal injection of clindamycin (10 mg/kg in 200 μL), prepared in 1× PBS and filter-sterilized.

Twenty-four hours after clindamycin administration, mice were moved from the large rat cage into smaller mouse cages, housing 4 mice per cage, and were inoculated via oral gavage with 1×10^6 *C. difficile* spores in 200 μL of 1× PBS. At the time of oral gavage, baseline weights were recorded by transferring mice using large forceps into sterile plastic Nalgene cups and weighing them on a digital scale inside a biosafety cabinet.

Following inoculation, mice were monitored daily and weighed using the same procedure for either 2 or 14 days. At the experimental endpoint, mice were euthanized by isoflurane anesthesia followed by cervical dislocation. Tissues were collected as needed.

CFU enumeration

Upon sacrifice, cecal contents were collected into pre-weighed 1.5 mL Eppendorf tubes for *C. difficile* biomass quantification. The tubes were reweighed to calculate the mass of the collected content. Tubes were then transferred into an anaerobic chamber, where 1 mL of pre-

reduced 1× PBS was added to each to resuspend the cecal content. After thorough homogenization, 10 μL of the suspension was added to 90 μL of 1× PBS in the first well of a 96-well plate to begin a series of seven 10-fold serial dilutions. For each subsequent dilution, 10 μL was transferred into 90 μL of PBS in the next well, mixing thoroughly at each step. From each dilution, 5 μL was spotted onto TCCFA plates to select for *C. difficile*. Plates were incubated for 24 h in the anaerobic chamber, after which colony-forming units (CFUs) were counted and normalized to the mass of the original cecal content.

Competition assays

Mice were infected with a total of 1×10^6 *C. difficile* spores, consisting of a 1:1 mixture of two strains: either wild-type and a fluorescent reporter strain, or two distinct fluorescent reporter strains (mNeonGreen and mScarlet-I3). Infections were performed as described above, and mice were sacrificed 48 h post-infection. Cecal contents were collected, weighed, and processed by resuspending in 1 mL of 1xPBS in the anaerobic chamber. Once the pellet was completely resuspended, ten-fold serial dilutions were prepared, and 100 μL of dilutions 4–7 were plated onto TCCFA plates to select for *C. difficile*.

After 24 h of anaerobic incubation, single colonies were picked using a pipette tip and resuspended in 200 μL of 1× PBS in 96-well plates (one plate per mouse). Plates were incubated at 37 °C for at least 1 h to allow fluorophore maturation. Fluorescence was then measured using a Synergy H1 Microplate Reader (excitation: 570 nm, emission: 600 nm). Wells with a positive fluorescence signal were identified as *mScarlet-I3*-expressing colonies, while wells lacking a signal represented either wild-type or mNeonGreen-expressing colonies. The ratio of mScarlet-I3 to mNeonGreen colonies recovered from each mouse was normalized to the input spore ratio.

Mouse colon tissue preparation

After mice were sacrificed, the entire colon was removed and placed into a 4% wt/vol paraformaldehyde and 1x PBS solution for 4 h. Following the 4-h tissue fixation, cross-sections of tissue were prepared by cutting 5 mm transverse rings. The tissues were then placed in O.C.T. Compound (Tissue-Tek) in Seal'N Freeze Cryotray tissue cassettes (Electron Microscopy Sciences) and flash frozen in a dry ice 100% ethanol bath. Frozen blocks were then processed by the Tufts Animal Histology Core, where 10 μm sections were cryosectioned and mounted to slides. Any remaining tissue that was not embedded was placed in 1x PBS for long-term storage. Mounted slides were kept at −80 °C until they were ready to be stained and imaged.

Staining mouse colon slides

Mounted slides were removed from the freezer and placed on the bench at room temperature for 30 min, and then an ImmEdge Pen (Vector Laboratories) hydrophobic marker was used to trace around the tissue sections to facilitate staining of the sections. Slides were blocked with blocking buffer (1x PBS, 3% BSA [w/v], 0.1% Triton X-100) for 30 min. Blocking buffer was then discarded, and stain containing blocking buffer, DAPI (100 ng/mL), and Phalloidin CruzFluor™ 647 (1:100) were added for 45 min. Following staining, slides were washed with blocking buffer 3X for 5 min before mounting with Prolong Diamond mounting medium. Slides were left to cure overnight at room temperature before imaging the following day.

Fluorescence microscopy

All images were acquired using a Leica DMi8 Thunder imager equipped with an HC PL APO 63×/1.4 numerical aperture (NA) phase-contrast oil immersion objective (in vitro microscopy) or an HC PL APO 20x/0.80 dry objective (mouse tissue sections). Excitation light was generated by a Lumencor Spectra-X multi-LED light source with integrated excitation filters. For all fluorescent channels, an XLED-QP quadruple-band dichroic beam-splitter (Leica) was used along with an external filter wheel (Leica). Phase-contrast images were taken with a 50-ms exposure time. mScarlet(I3) was excited at 550 nm (33% intensity) with 200 ms exposure time, a dichroic mirror at 570 nm, and the emitted light was filtered using a 595/40 nm emission filter (Leica). mNeonGreen was excited at 470 nm with a 300 ms exposure, a dichroic mirror at 419 nm, and the emitted light was filtered using a 515/40 nm emission filter. Emitted and transmitted light was detected using a Leica DFC 9000 GTC sCMOS camera. All strains for a given experiment were spotted and captured sequentially on the same agarose pad.

For imaging mouse colonic tissue, stained slides were imaged using the same Leica microscope as indicated above, using a 20x dry objective lens. DAPI stain for visualizing colonic epithelial cell nuclei was excited at 395 nm (10% intensity) with a 50-ms exposure, dichroic mirror at 415 nm, and emitted light was filtered using a 430/36-nm emission filter (Leica). The phalloidin F-actin stain was excited at 640 nm, a dichroic mirror at 660 nm, and the emitted light was collected at 720/50 nm. Cells containing either mScarlet(I3) or mNeonGreen fluorescent proteins were imaged as described above. 5 μm step sizes were used to image through the colon tissue.

Image analysis and quantification

After image acquisition, images were processed using Leica Instant Computational Clearing (ICC) to eliminate bleed-through of fluorescent signals into neighboring cells. The adaptive strategy was executed with a feature scale of 2500 nm and 98% strength. Following ICC, images were exported from Leica's LASX software and further processed in FIJI. Specifically, images were cropped to remove out-of-focus regions, and the best-focused Z-plane was selected for each channel to correct for chromatic aberration.

Quantitative analysis of broth-grown cells was performed using the SuperSegger[64] pipeline in MATLAB with the provided 60× analysis settings. The resulting clist matrices, which contained single-cell data, were exported from MATLAB. For display purposes, image scaling was uniformly adjusted for brightness and contrast across all strains in each experiment (unless marked "ADJUSTED" on the image). At least three images per strain were captured in each replicate, and every strain was analyzed using three biological replicates, with image analysis performed on at least two positions per replicate.

To quantify the proportion and magnitude of *C. difficile* toxin gene expression in situ during infection, *C. difficile* cells were first identified using the mScarlet-I3 channel. Median fluorescence intensity for each cell was then measured in both the mScarlet-I3 and mNeonGreen channels. This approach minimizes selection bias by including all identified cells, not just those with the highest mNeonGreen signal. Individual cells were manually traced along their full length using segmented lines in FIJI. The P_{tcdA}*::mNG* signal for each cell was normalized to its corresponding P_{cwp2}*::LP-mScI3** signal. This normalization reduced variability due to factors such as slight defocusing or occlusion by debris, which can artificially lower raw fluorescence values. For each experimental group, cross-sectional images of the colon were analyzed from at least three different mice. A minimum of 100 cells per image was measured.

To classify cells as "Toxin-ON," the normalized mNeonGreen fluorescence from the toxin-null Δ*tcdR* dual reporter strain was used as a baseline. The highest fluorescence value observed in the Δ*tcdR* population was used as the threshold for Toxin-ON classification. Cells with fluorescence values exceeding this threshold were defined as Toxin-ON. Cells within the Δ*tcdR* population that were above the clustering of the datapoints were classified as Toxin-ON. Thresholds were determined independently for Day 2 and Day 14 post-infection. For spatial localization analysis, cells were categorized into three groups: luminal, mucosal, and epithelial. Luminal cells were defined as those located in the central lumen of the colonic cross-section. Mucosal cells formed a distinct border adjacent to the epithelium (>50 μm), as determined by F-actin phalloidin staining. Cells that were

in direct contact with the epithelial layer, i.e., where the mScarlet-I3 signal co-localizes with phalloidin, were classified as epithelial-associated.

Cell curvature and length measurements

To assess cell curvature, segmented lines were manually drawn along the length of individual *C. difficile* cells using FIJI (ImageJ) based on the mScarlet-I3 fluorescence signal from reporter strains. The total length of each segmented line was recorded to represent the cell's actual path length. X and Y coordinates of the cell endpoints were extracted and used to calculate the Euclidean distance between the two ends of each cell using a FIJI plugin. A curvature ratio was then calculated by dividing the total segmented length by the Euclidean distance. Cells with curvature ratios greater than 1.03 were classified as curved.

Statistics and reproducibility

No statistical method was used to predetermine sample size. No data were excluded from the analyses. All in vitro experiments were done a minimum of three times. Mouse experiments with animals infected with the following strains consisted of the indicated replicates: P_{gluD}::*mNG* (1), P_{gluD}::*mScI3* (1), P_{slpA}::*mNG* (2), P_{slpA}::*mScI3* (1), P_{cwp2}::*LP-mScI3* (2), WT vs P_{cwp2}::*LP-mScI3* (2), WT vs P_{gluD}::*mScI3* (1), WT vs P_{slpA}::*mScI3* (1), P_{cwp2}::*LP-mScI3* vs P_{slpA}::*mNG* (3), P_{gluD}::*mScI3* vs P_{gluD}::*mNG* (2), WT unmarked (6), WT-P_{cwp2}::*LP-mScI3* /P_{tcdA}::*mNG* (4), Δ*tcdR*-P_{cwp2}::*LP-mScI3* /P_{tcdA}::*mNG* (3), Δ*rstA*-P_{cwp2}::*LP-mScI3* /P_{tcdA}::*mNG* (5), Δ*rstA*-P_{cwp2}::*LP-mScI3* (1), Δ*rstA* (1), Δ*rstA*/*rstA* (1), and Δ*rstA*Δ*tcdR*-P_{cwp2}::*LP-mScI3* /P_{tcdA}::*mNG* (1).

To quantify both the proportion and magnitude of *C. difficile* toxin gene expression in situ during infection, individual *C. difficile* cells were first identified using the mScarlet-I3 channel. For each identified cell, the median fluorescence intensity was then measured in both the mScarlet-I3 and mNeonGreen channels. This unbiased approach ensures that all detected bacteria are included in the analysis, rather than selectively focusing on cells with high mNeonGreen signal, thereby providing an accurate representation of toxin gene expression across the population.

Reporting summary

Further information on research design is available in the Nature Portfolio Reporting Summary linked to this article.

Data availability

Data used to generate graphs, exact *P* values from statistical analyses, and uncropped scans of blots can be found within the Supplementary Data/Supplementary Information file or source data file. Raw image files have been deposited in FigShare and can be accessed using the doi 10.6084/m9.figshare.29066990. Plasmids generated to make the strains in this article were deposited with Addgene and are available under the corresponding accession numbers: pMTL-YN1C Promoterless *mNeonGreen* (Addgene ID: 251223), pMTL-YN1C P_{tcdA}::*mNeonGreen* (Addgene ID: 251224), pMTL-YN1C P_{slpA}::*mNeonGreen* (Addgene ID: 251225), and pMTL-YN1C P_{cwp2}::*LP-mScI3 (G228R)* (Addgene ID: 251226). *E. coli* and *C. difficile* strains described in this study are available upon request from the corresponding author. Source data are provided with this paper.

Code availability

No code was developed specifically for the analyses presented here. All software tools used for bioinformatic analyses are listed in the Methods.

References

1. Arnaouteli, S., Bamford, N. C., Stanley-Wall, N. R. & Kovács, ÁT. *Bacillus subtilis* biofilm formation and social interactions. *Nat. Rev. Microbiol.* **19**, 600–614 (2021).
2. Soavelomandroso, A. P. et al. Biofilm structures in a mono-associated mouse model of *Clostridium difficile* infection. *Front. Microbiol.* **8**, 2086 (2017).
3. Sinha, R., Ottosen, E. N., Ngwaga, T., Shames, S. R. & DiRita, V. J. Carbapenem-resistant *Enterobacter hormaechei* uses mucus metabolism to facilitate gastrointestinal colonization. *mBio* **16**, e0288424 (2025).
4. Madhu, B., Miller, B. M. & Levy, M. Single-cell analysis and spatial resolution of the gut microbiome. *Front. Cell Infect. Microbiol.* **13**, 1271092 (2023).
5. McCallum, G. & Tropini, C. The gut microbiota and its biogeography. *Nat. Rev. Microbiol.* **22**, 105–118 (2024).
6. Valm, A. M. et al. Systems-level analysis of microbial community organization through combinatorial labeling and spectral imaging. *Proc. Natl. Acad. Sci. USA* **108**, 4152–4157 (2011).
7. Mondragón-Palomino, O. et al. Three-dimensional imaging for the quantification of spatial patterns in microbiota of the intestinal mucosa. *Proc. Natl. Acad. Sci. USA* **119**, e2118483119 (2022).
8. Sarfatis, A., Wang, Y., Twumasi-Ankrah, N. & Moffitt, J. R. Highly multiplexed spatial transcriptomics in bacteria. *Science* **387**, eadr0932 (2025).
9. Gallego-Hernandez, A. L. et al. Upregulation of virulence genes promotes *Vibrio cholerae* biofilm hyperinfectivity. *Proc. Natl. Acad. Sci. USA* **117**, 11010–11017 (2020).
10. Davis, K. M., Mohammadi, S. & Isberg, R. R. Community behavior and spatial regulation within a bacterial microcolony in deep tissue sites serves to protect against host attack. *Cell Host Microbe* **17**, 21–31 (2015).
11. Sorobetea, D. et al. Inflammatory monocytes promote granuloma control of *Yersinia* infection. *Nat. Microbiol.* **8**, 666–678 (2023).
12. Magoulopoulou, A. et al. Spatial resolution of Mycobacterium tuberculosis bacteria and their surrounding immune environments based on selected key transcripts in mouse lungs. *Front. Immunol.* **13**, 876321 (2022).
13. Lavin, R. C. & Tan, S. Spatial relationships of intra-lesion heterogeneity in *Mycobacterium tuberculosis* microenvironment, replication status, and drug efficacy. *PLoS Pathog.* **18**, e1010459 (2022).
14. Donaldson, G. P., Lee, S. M. & Mazmanian, S. K. Gut biogeography of the bacterial microbiota. *Nat. Rev. Microbiol.* **14**, 20–32 (2016).
15. Nava, G. M., Friedrichsen, H. J. & Stappenbeck, T. S. Spatial organization of intestinal microbiota in the mouse ascending colon. *ISME J.* **5**, 627–638 (2011).
16. Shi, H. et al. Highly multiplexed spatial mapping of microbial communities. *Nature* **588**, 676–681 (2020).
17. Whitaker, W. R., Shepherd, E. S. & Sonnenburg, J. L. Tunable expression tools enable single-cell strain distinction in the gut microbiome. *Cell* **169**, 538–546.e12 (2017).
18. Hill, C. A. et al. Bacteroides fragilis toxin expression enables lamina propria niche acquisition in the developing mouse gut. *Nat. Microbiol.* **9**, 85–94 (2024).
19. Anderson, M. C., Vonaesch, P., Saffarian, A., Marteyn, B. S. & Sansonetti, P. J. *Shigella sonnei* encodes a functional T6SS used for interbacterial competition and niche occupancy. *Cell Host Microbe* **21**, 769–776.e3 (2017).
20. Guo, Y., Kitamoto, S. & Kamada, N. Microbial adaptation to the healthy and inflamed gut environments. *Gut Microbes* **12**, 1857505 (2020).
21. Trzilova, D. & Tamayo, R. Site-specific recombination—how simple DNA inversions produce complex phenotypic heterogeneity in bacterial populations. *Trends Genet.* **37**, 59–72 (2021).
22. Krinos, C. M. et al. Extensive surface diversity of a commensal microorganism by multiple DNA inversions. *Nature* **414**, 555–558 (2001).

23. Koirala, S. et al. A nutrient-tunable bistable switch controls motility in *Salmonella enterica* serovar Typhimurium. *mBio* **5**, e01611–e01614 (2014).
24. Gory, R., Personnic, N. & Blaha, D. Unravelling the roles of bacterial nanomachines bistability in pathogens' life cycle. *Microorganisms* **12**, 1930 (2024).
25. Anjuwon-Foster, B. R. & Tamayo, R. A genetic switch controls the production of flagella and toxins in *Clostridium difficile*. *PLoS Genet.* **13**, e1006701 (2017).
26. Koenigsknecht, M. J. et al. Dynamics and establishment of *Clostridium difficile* infection in the murine gastrointestinal tract. *Infect. Immun.* **83**, 934–941 (2015).
27. Ransom, E. M., Kaus, G. M., Tran, P. M., Ellermeier, C. D. & Weiss, D. S. Multiple factors contribute to bimodal toxin gene expression in *Clostridioides* (*Clostridium*) *difficile*. *Mol. Microbiol.* **110**, 533–549 (2018).
28. Buddle, J. E. & Fagan, R. P. Pathogenicity and virulence of *Clostridioides difficile*. *Virulence* **14**, 2150452 (2023).
29. Engevik, M. A. et al. Human *Clostridium difficile* infection: altered mucus production and composition. *Am. J. Physiol. Gastrointest. Liver Physiol.* **308**, G510–G524 (2015).
30. Bagdasarian, N., Rao, K. & Malani, P. N. Diagnosis and treatment of *Clostridium difficile* in adults: a systematic review. *JAMA* **313**, 398–408 (2015).
31. Carroll, K. C. & Mizusawa, M. Laboratory tests for the diagnosis of *Clostridium difficile*. *Clin. Colon Rectal Surg.* **33**, 73–81 (2020).
32. Donnelly, M. L. et al. Development of a dual-fluorescent-reporter system in *Clostridioides difficile* reveals a division of labor between virulence and transmission gene expression. *mSphere* **7**, e0013222 (2022).
33. Nhu, N. T. Q. et al. Flagellar switch inverted repeats impact heterogeneity in flagellar gene expression and thus C. difficile RT027/MLST1 virulence. *Cell Reports* **44**, 115830 (2025).
34. Gadella, T. W. J. et al. mScarlet3: a brilliant and fast-maturing red fluorescent protein. *Nat. Methods* **20**, 541–545 (2023).
35. Howerton, A., Patra, M. & Abel-Santos, E. Fate of ingested *Clostridium difficile* spores in mice. *PLoS ONE* **8**, e72620 (2013).
36. Semenyuk, E. G. et al. Analysis of bacterial communities during *Clostridium difficile* infection in the mouse. *Infect. Immun.* **83**, 4383–4391 (2015).
37. Hasegawa, Y., Mark Welch, J. L., Rossetti, B. J. & Borisy, G. G. Preservation of three-dimensional spatial structure in the gut microbiome. *PLoS ONE* **12**, e0188257 (2017).
38. Tropini, C., Earle, K. A., Huang, K. C. & Sonnenburg, J. L. The gut microbiome: connecting spatial organization to function. *Cell Host Microbe* **21**, 433–442 (2017).
39. Majumdar, A. & Govind, R. Regulation of *Clostridioides difficile* toxin production. *Curr. Opin. Microbiol.* **65**, 95–100 (2022).
40. Edwards, A. N., Anjuwon-Foster, B. R. & McBride, S. M. RstA is a major regulator of *Clostridioides difficile* toxin production and motility. *mBio* **10**, https://doi.org/10.1128/mbio.01991-18 (2019).
41. Edwards, A. N., Tamayo, R. & McBride, S. M. A novel regulator controls *Clostridium difficile* sporulation, motility and toxin production. *Mol. Microbiol.* **100**, 954–971 (2016).
42. Ticer, T. D. et al. Bacterial metabolites influence the autofluorescence of *Clostridioides difficile*. *Front. Microbiol.* **15**, 1459795 (2024).
43. Fletcher, J. R. et al. *Clostridioides difficile* exploits toxin-mediated inflammation to alter the host nutritional landscape and exclude competitors from the gut microbiota. *Nat. Commun.* **12**, 462 (2021).
44. Phillips, Z. N., Tram, G., Seib, K. L. & Atack, J. M. Phase-variable bacterial loci: how bacteria gamble to maximise fitness in changing environments. *Biochem. Soc. Trans.* **47**, 1131–1141 (2019).
45. Diard, M. et al. Stabilization of cooperative virulence by the expression of an avirulent phenotype. *Nature* **494**, 353–356 (2013).
46. Kint, N. et al. The σB signalling activation pathway in the enteropathogen *Clostridioides difficile*. *Environ. Microbiol.* **21**, 2852–2870 (2019).
47. Morawska, L. P., Hernandez-Valdes, J. A. & Kuipers, O. P. Diversity of bet-hedging strategies in microbial communities—recent cases and insights. *WIREs Mech. Dis.* **14**, e1544 (2022).
48. Kint, N., Morvan, C. & Martin-Verstraete, I. Oxygen response and tolerance mechanisms in *Clostridioides difficile*. *Curr. Opin. Microbiol.* **65**, 175–182 (2022).
49. Castro-Córdova, P. et al. Entry of spores into intestinal epithelial cells contributes to recurrence of *Clostridioides difficile* infection. *Nat. Commun.* **12**, 1140 (2021).
50. Fung, C. et al. High-resolution mapping reveals that microniches in the gastric glands control *Helicobacter pylori* colonization of the stomach. *PLoS Biol.* **17**, e3000231 (2019).
51. Dong, Q. et al. Protection against *Clostridioides difficile* disease by a naturally avirulent strain. *Cell Host Microbe* **33**, 59–70.e4 (2025).
52. Donadoni, C. et al. Improvement of combined FISH and immunofluorescence to trace the fate of somatic stem cells after transplantation. *J. Histochem. Cytochem.* **52**, 1333–1339 (2004).
53. Hirano, M. et al. A highly photostable and bright green fluorescent protein. *Nat. Biotechnol.* **40**, 1132–1142 (2022).
54. Campbell, B. C., Paez-Segala, M. G., Looger, L. L., Petsko, G. A. & Liu, C. F. Chemically stable fluorescent proteins for advanced microscopy. *Nat. Methods* **19**, 1612–1621 (2022).
55. Campbell, B. C. et al. mGreenLantern: a bright monomeric fluorescent protein with rapid expression and cell filling properties for neuronal imaging. *Proc. Natl. Acad. Sci. USA* **117**, 30710–30721 (2020).
56. Müh, U., Pannullo, A. G., Weiss, D. S. & Ellermeier, C. D. A xylose-inducible expression system and a crispr interference plasmid for targeted knockdown of gene expression in *Clostridioides difficile*. *J. Bacteriol.* **201**, e00711–e00718 (2019).
57. Omorotionmwan, B. B. et al. Chromosomal engineering of inducible isopropanol-butanol-ethanol production in *Clostridium acetobutylicum*. *Front. Bioeng. Biotechnol.* **11**, 1218099 (2023).
58. Heap, J. T., Pennington, O. J., Cartman, S. T., Carter, G. P. & Minton, N. P. The ClosTron: a universal gene knock-out system for the genus *Clostridium*. *J. Microbiol. Methods* **70**, 452–464 (2007).
59. Jin, W.-B. et al. Genetic manipulation of gut microbes enables single-gene interrogation in a complex microbiome. *Cell* **185**, 547–562.e22 (2022).
60. Arnold, J., Glazier, J. & Mimee, M. Genetic engineering of resident bacteria in the gut microbiome. *J. Bacteriol.* **205**, e0012723 (2023).
61. Lopetuso, L. R., Scaldaferri, F., Petito, V. & Gasbarrini, A. Commensal Clostridia: leading players in the maintenance of gut homeostasis. *Gut Pathog.* **5**, 23 (2013).
62. Ng, Y. K. et al. Expanding the repertoire of gene tools for precise manipulation of the *Clostridium difficile* genome: allelic exchange using pyrE alleles. *PLoS ONE* **8**, e56051 (2013).
63. Karasawa, T., Ikoma, S., Yamakawa, K. & Nakamura, S. A defined growth medium for *Clostridium difficile*. *Microbiology* **141**, 371–375 (1995).
64. Stylianidou, S., Brennan, C., Nissen, S. B., Kuwada, N. J. & Wiggins, P. A. SuperSegger: robust image segmentation, analysis and lineage tracking of bacterial cells. *Mol. Microbiol.* **102**, 690–700 (2016).

Acknowledgements

We thank Nathan Li, Terance Cheung, and the staff of the Tufts Animal Histology core for their insight and guidance with tissue processing and

slide staining, as well as their work in preparing slides for microscopy. We thank John Ribis for cloning the original *mNeonGreen* and *mScarlet* sequences. We also thank Shumin Tan for her expertise and guidance in the microscopy of murine colonic tissue sections. This work was funded by the National Institutes of Health, National Institute of Allergy and Infectious Diseases (Division of Intramural Research of the NIAID) R21AI168849 to AS and CAK; T32AI007422 and F31AI191587 to NVD; and a Burroughs Wellcome Fund Investigators in the Pathogenesis of Disease grant.

Author contributions

N.V.D., M.L.D.M., C.A.K., and A.S. contributed to the conceptualization and overall design of the study. N.V.D. and M.L.D.M. generated the *C. difficile* strains used within the study. N.V.D. performed all the experiments, carried out the data analysis, and generated all the figures. N.V.D. and A.S. wrote and revised the manuscript. All authors (N.V.D., M.L.D.M., C.A.K., and A.S.) reviewed, provided feedback on, and approved the final version of the manuscript.

Competing interests

The authors declare no competing interests.

Additional information

Supplementary information The online version contains supplementary material available at https://doi.org/10.1038/s41467-026-68411-6.

Correspondence and requests for materials should be addressed to Aimee Shen.

Peer review information *Nature Communications* thanks the anonymous reviewers for their contribution to the peer review of this work. A peer review file is available.